MOLECULAR IMAGING AND BIOLOGY

Mol Imaging Biol (2019) 21:686–695
DOI: 10.1007/s11307-018-1280-1

Published Online: 24 September 2018

RESEARCH ARTICLE

Whole Body PET Imaging with a Norepinephrine Transporter Probe 4-[^{18}F]Fluorobenzylguanidine: Biodistribution and Radiation Dosimetry

Stephen J. Lokitz,[1] Sudha Garg,[1,2] Rachid Nazih,[1,2] Pradeep K. Garg[1,2]

[1]*Center for Molecular Imaging and Therapy, Biomedical Research Foundation, Shreveport, LA, 71103, USA*
[2]*Department of Radiology, Wake Forest University Health Science, Winston Salem, NC, USA*

Abstract

Purpose: 4-[^{18}F]Fluorobenzylguanidine ([^{18}F]PFBG) is a positron emission tomography (PET) probe for non-invasive targeting of the norepinephrine transporter. The aim of this study was to assess uptake and distribution characteristics of this PET probe.

Procedures: Three cynomolgus monkeys were injected with 269 ± 51 MBq (7.3 ± 1.4 mCi) of [^{18}F]PFBG and 21 whole body PET scans were acquired over 165 min. s around organs to generate time-activity curves. The absorbed doses to individual organs and the effective dose to the whole body were estimated.

Results: Favorable distribution of [^{18}F]PFBG was noted with a fast wash-in and wash-out of radioactivity from several tissues. [^{18}F]PFBG rapidly distributed in the heart, liver, kidneys, and adrenal glands. The uptake presented as %ID in the brain, lung, and spleen was 1.06 ± 0.45, 6.28 ± 0.33, and 1.39 ± 0.35 at 1 min and decreased to 0.29 ± 0.02, 1.78 ± 0.31, and 0.66 ± 0.22 by 112 min. In general, a two- to fourfold reduction was noted from peak radioactivity levels. Rapid uptake and significant retention of radioactivity was noted in the heart and the septal wall was distinctly visible by 20 min. Fast wash-in and washout kinetics for [^{18}F]PFBG resulted in shorter residence times. The residence time for the liver, lungs, kidneys, and spleen were 28.01 ± 7.73 min, 2.97 ± 0.56 min, 6.04 ± 3.41 min, and 1.09 ± 0.33 min, respectively. The mean effective dose for the 70-kg male was 0.04 ± 0.00 mSv/MBq. The organs receiving the highest radiation dose in the 70-kg male model were the testes (0.11 ± 0.02 mGy/MBq), adrenals (0.08 ± 0.01 mGy/MBq), and urinary bladder wall (0.08 ± 0.01 mGy/MBq).

Conclusions: [^{18}F]PFBG shows a favorable biodistribution pattern. Rapid and persistent uptake was noted in innervated organs. Renal clearance was the major path for elimination of [^{18}F]PFBG. The estimated radiation burden from [^{18}F]PFBG was significantly lower than that from [^{124}I]MIBG.

Key words: 4-[^{18}F]Fluorobenzylguanidine, PET imaging, Biodistribution in primates, Radiation dose estimates

Introduction

Metaiodobenzylguanidine (MIBG), a guanethidine analogue, is a functional analogue of norepinephrine (NE) with its transport, storage, and release process mimicking NE [1]. MIBG binds to the cell membrane and internalizes *via* an active transport mechanism for subsequent storage in the vesicles [2]. The radioiodinated analogue [^{131}I]MIBG was initially developed for the treatment and scintigraphy of the adrenal medulla [3]. Further utilization of [^{131}I]MIBG and

Correspondence to: Pradeep Garg; *e-mail:* Pradeep.Garg@cmitla.org

[^{123}I]MIBG showed promising results for the assessment of cardiomyopathy and myocardial infarction [4, 5]. In addition, radioiodinated MIBG has also been effective in targeting neuroendocrine tumors such as neuroectodermal [6], pheochromocytoma [7–9], neuroblastoma [9], carcinoid [10], and medullary thyroid carcinoma [11]. The use of single-photon emission computed tomography imaging (SPECT) with [^{123}I]MIBG offered higher sensitivity for lesion detection in clinical studies as compared to planar imaging using [^{131}I]MIBG [7, 12]. Emergence of the more advanced imaging technology positron emission tomography (PET) for routine clinical use stimulated interest in developing PET analogues of [*I]MIBG. As with SPECT, PET offers tomographic imaging capabilities and provides superior spatial resolution but adds rigorous attenuation correction for fully quantitative data. Initially, [^{124}I]-MIBG was developed as a PET analogue. While an attractive option, the long half-life ($t_{1/2}$ = 4.18 days) and complex decay schema of I-124 including high energy gamma rays [13] lead to higher radiation dose to humans, limiting the administered dose [14]. Additionally, delayed imaging post injection is recommended for acceptable quality images [13, 14]. To overcome such limitations, we and many others focused on developing ^{18}F-labeled MIBG analogues for PET imaging of norepinephrine transporters (NET). Towards that goal, among many compounds, *para*-[^{18}F]fluorobenzylguanidine ([^{18}F]PFBG), *meta*-[^{18}F]fluorobenzylguanidine ([^{18}F]MFBG), and 4-[^{18}F]fluoro-3-iodobenzylguanidine ([^{18}F]FIBG) were developed [15, 16]. *In vitro* and *in vivo* evaluations of these newly developed fluorinated benzylguanidines showed superior uptake and retention properties over that of [^{123}I/^{131}I]MIBG. Besides the inherent advantages of PET imaging, the higher specific activity of fluorobenzylguanidines from the no-carrier added synthesis may have further contributed towards their superior targeting abilities [15–17]. Fluorobenzylguanidines are also less lipophilic and not susceptible to *in vivo* dehalogenation due to the stronger carbon-fluorine bond compared to the carbon-iodine bond in [*I]MIBG which further aids improved biological characteristics [18]. Therefore, ^{18}F-labeled fluorobenzylguanidine analogues are relevant probes to target NET in humans.

The results from preclinical studies with [^{18}F]PFBG and [^{18}F]MFBG have shown promising results [16, 17, 19–21]. A recent first-in-human study with [^{18}F]MFBG [22] further demonstrates the relevance of fluorobenzylguanidine. While recent efforts by the Lewis group have modified the synthesis for [^{18}F]MFBG, the overall yields remain ~ 6-fold lower than that for [^{18}F]PFBG and necessitate the use of ~ 11.1 GBq (300 mCi) of [^{18}F]fluoride for each 370 MBq (10 mCi) dose of [^{18}F]MFBG [17]. Since both [^{18}F]PFBG and [^{18}F]MFBG isomers exhibit similar biological traits *in vitro* and *in vivo*, the ability to synthesize [^{18}F]PFBG at significantly higher yields [16, 17] offers a distinct advantage to explore its translational and clinical potential [15–17]. In a previously conducted study in canines with pheochromocytoma, [^{18}F]PFBG distinctly localized neuroendocrine tumor on PET scans with tumor standardized uptake values > 16 [20]. In a different canine study, [^{18}F]PFBG demonstrated the impact of transient ischemia on myocardial sympathetic innervation [21, 23]. Results from such studies demonstrate the significant clinical potential of [^{18}F]PFBG. While [^{18}F]MFBG could play a unique role in certain clinical applications, the combination of the facile radiochemical synthesis of [^{18}F]PFBG and comparable biological characteristics of the two analogues allude to a distinct advantage in choosing [^{18}F]PFBG for clinical and translational studies [16, 17].

The potential of [^{18}F]PFBG in clinical and translational studies underscores the need to conduct the whole-body distribution study in primates and to provide radiation dose estimates for this radiopharmaceutical in humans [13, 24]. Herein, we report the results from whole-body PET imaging study conducted in non-human primates using [^{18}F]PFBG.

Materials and Methods

This study was reviewed and approved by the Institutional Animal Care and Use Committee (IACUC) of the Wake Forest University Health Sciences (WFUHS) in compliance with the National Institute of Health guidance on the use of laboratory animals. Environmental enrichment was provided as outlined in the WFUHS IACUC Non-Human Primate Environmental Enrichment Plan. Three male cynomolgus monkeys (*Macaca fascicularis*) with an average weight of 6.5 ± 1.6 kg (range 5.0–8.2 kg) and a median age of 15 years (11–20 years) were included in this study. Prior to the PET scans, the animals were anesthetized with ketamine (8 mg/kg) and intubated. The anesthesia was maintained throughout the imaging session using isoflurane (1.5 %). A catheter was placed intravenously to administer [^{18}F]PFBG.

Synthesis of [^{18}F]PFBG

The synthesis of [^{18}F]PFBG was performed using a previously described method [16]. Briefly, 4-cyano-N,N,N-trimethylbenzenaminium trifluoromethane sulfonate was reacted with [^{18}F] tetrabutylammonium *tert*-butyl ammonium fluoride. The resultant 4-[^{18}F] fluorobenzonitrile was reduced with lithium aluminum hydride followed by the reaction of the resultant benzylamine intermediate with 2-methyl 2-thiopseudourea sulfate. The crude product thus obtained was purified using high performance liquid chromatography (HPLC) and was reconstituted in saline solution.

PET Imaging

PET images were acquired on an Advance NXi PET scanner (General Electric Medical Systems, Wisconsin, USA) operating in 3D mode. The performance characteristics of this scanner have been described previously [25–27]. The

axial field of view covers 15.2 cm and each bed position includes 35 slices with 4.25 mm axial slice thickness. Images were reconstructed using the ADVANCE 3D iterative reconstruction algorithm with 2 iterations and 28 subsets and attenuation, delayed random, and scatter corrections applied [28, 29]. Standard quantification techniques allowed the pixel values to be represented as radioactivity concentration (kBq/ml).

After sedation, the non-human primates ($n = 3$) were positioned on the scanner table. An isotope transmission scan using ^{68}Ge pin sources was acquired (3 min per bed position) for attenuation correction purposes. Subsequently, 269 ± 51 MBq (7.3 ± 1.4 mCi) of [^{18}F]PFBG was administered intravenously and a dynamic series of PET images were acquired from top of the head to the knees (four or five bed positions depending on animal size) over 165 min. Overall, twenty-one dynamic frames were acquired using the following timing sequence: 4 × 15 s/bed, 3 × 30 s/bed, 6 × 60 s/bed, 5 × 120 s/bed, and 3 × 240 s/bed with added frames for animal 1 (1 × 240 s/bed) and animal 3 (2 × 240 s/bed) to accommodate their longer body size. All images were analyzed using PMOD 3.206 (PMOD Technologies, Zurich, Switzerland).

PET Image Analysis

Initially, a large region of interest (ROI) was drawn on the axial views of the PET images such that the entire visible body was included in the ROI to estimate the percent of injected radioactivity recovered. Additional ROIs were placed manually on identifiable organs to obtain the amount of radioactivity present in those organs at each time point. Each ROI was carefully placed to minimize any overlap with adjacent organs and was reverified by viewing through axial, coronal, and sagittal image planes. Additionally, the temporal frames were summed to obtain a high-count image set for assessing the accuracy of ROI placement and organ identification.

The lumbar spine was used to estimate the total radioactivity in the red marrow using a previously published method [30]. Total radioactivity in the adrenal glands was calculated by doubling the radioactivity in the left adrenal gland to account for the left and the right adrenal glands. Radioactivity accumulation in muscle was estimated by multiplying the radioactivity concentration obtained from a ROI placed in the thigh muscles with the total estimated muscle mass following a previously described method [31].

Time activity curves (TACs) were generated from the ROIs placed on organs delineated on the PET images. The total mass for individual organs was estimated as described previously [32]. The radioactivity accumulation was expressed as percent injected dose (%ID). The residence times were obtained by performing numerical integration utilizing the trapezoidal method from time zero to the last imaged time point. The radioactivity from last imaged time point to infinity was assumed to deplete solely *via* physical decay without any further biological clearance [31, 33] and was analytically integrated. The number of disintegrations per unit activity for the identified source organs, which is mathematically equivalent to the residence times, were entered into OLINDA/EXM 1.0 software [31, 34] to obtain the organ absorbed dose, effective dose equivalent (EDE), and effective dose (ED) estimates for the 70-kg male, 15-year-old, 10-year old, 5-year old, and 1-year old phantoms using the 1-h bladder voiding model. Parameters for the bladder voiding model were extracted from the urinary bladder TAC which was used as a proxy to estimate the cumulated urinary excretion.

Statistical Analysis

Results are expressed as mean ± standard deviation. Statistical analysis was performed using the Student's *t* test for unpaired data. A 95 % confidence level was chosen to determine the significance of differences between groups, with a *p* value of less than 0.05 indicating a significant difference.

Results

The results from this study show a favorable distribution pattern for [^{18}F]PFBG in non-human primates with fast wash-in and wash-out of radioactivity from several organs including the blood pool, kidneys, spleen, and brain. A typical biodistribution profile for [^{18}F]PFBG is shown in Fig. 1. Axial, coronal, and sagittal views of the time-summed whole body [^{18}F]PFBG PET images fused with the Ge-68 isotope transmission scan from a representative non-human primate show significant uptake of radioactivity in the heart, salivary glands, liver, kidneys, and the bladder (Fig. 1). Biodistribution data derived from whole body PET scans are presented as %ID in various organs at 1, 30, 55, 86, and 112 min (Table 1).

A time sequence of the whole body maximum intensity projection images of a non-human primate injected with [^{18}F]PFBG show the biodistribution characteristics of [^{18}F]PFBG at various time points (Fig. 2). The heart, salivary glands, liver, spleen, and the kidneys are distinctly visible on these images as early as 1 and 5 min (Fig. 2a, b). After the clearance of radioactivity from the surrounding organs, the left adrenal gland became distinctly visible by 61 min (Fig. 2c).

Rapid arrival of radioactivity in the heart led to clear visualization of the heart (Fig. 3). Initially, the uptake in the heart represented blood pool activity (Fig. 3a). Rapid depletion of radioactivity from the blood pool resulted in clear delineation of the myocardial and septal wall by 20 min (Fig. 3b) which remained visible at later timepoints (Fig. 3c).

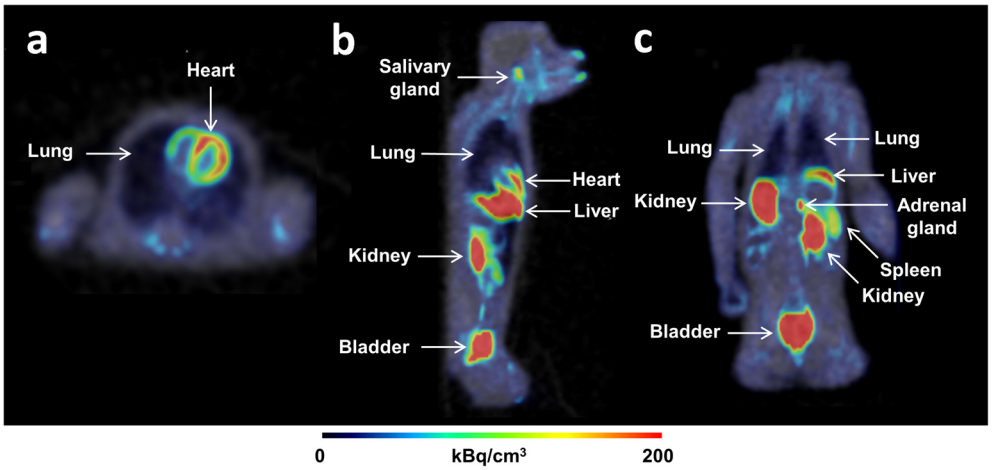

Fig. 1. Summed whole-body PET images from a representative non-human primate showing *in vivo* biodistribution of [^{18}F]PFBG after administration of 314 MBq (8.5 mCi) of [^{18}F]PFBG. Images represent **a** axial, **b** sagittal, and **c** coronal views, summed across all dynamic frames fused with the Ge-68 isotope transmission scan. Significant accumulation of [^{18}F]PFBG is seen in the heart, liver, bladder, and the kidneys.

The total radioactivity in the whole body was assessed by placing a large ROI encompassing the entire body on the first dynamic image set. This whole-body ROI accounted for 105 % ± 7 % of the administered dose. The radioactivity contents in individual organs were calculated by drawing individual ROIs over the organs that were easily visualized and identified on the PET images.

The accumulation and clearance of radioactivity in the kidneys and the urinary bladder is shown in Fig. 4. As seen from the TACs, an initial surge of radioactivity was noted in the kidneys within the first minute post-injection, followed a gradual excretion of radioactivity from the kidneys into the bladder. Accumulation in the bladder was initially low with less than five %ID accumulating in the bladder in the first 8 min. Thereafter, the radioactivity levels increased steadily in the bladder and > 30 %ID accumulated into the bladder over the course of this study.

The mean TACs for the liver, muscle, blood pool, lungs, spleen, and brain are shown in Fig. 5. In general, after the initial uptake, the radioactivity levels in most organs decreased significantly, except for the muscles. For example, the radioactivity levels in the blood pool peaked at 51.72 ± 4.40 %ID soon after administration (1 min) and rapidly decreased to 16.20 ± 9.00 %ID by 30 min, a 3-fold decrease. Similarly, the %ID in the brain, lung, and spleen decreased from 1.06 ± 0.45, 6.28 ± 0.33 and 1.39 ± 0.35, respectively at 1 min to 0.29 ± 0.02, 1.78 ± 0.31 and 0.66 ± 0.22, respectively by 112 min. In general, a two- to fourfold reduction was noted in most organs from their peak radioactivity levels with the notable exception of the muscle and urinary bladder.

The uptake and washout trend in the heart, pancreas, and salivary glands is shown in Fig. 6. The average uptake in the heart was 1.24 ± 0.06 %ID and 0.95 ± 0.11 %ID at 30 min and 112 min, respectively. The uptake in the pancreas was 0.95 ±

Table 1.. Biodistribution of [^{18}F]PFBG in non-human primates (%ID: mean ± standard deviation)

Organ	1 min	30 min	55 min	86 min	112 min
Adrenals	0.48 ± 0.25	0.33 ± 0.03	0.30 ± 0.02	0.29 ± 0.02	0.29 ± 0.02
Brain	1.06 ± 0.45	0.31 ± 0.03	0.29 ± 0.03	0.29 ± 0.03	0.29 ± 0.02
Blood pool	51.72 ± 4.40	16.20 ± 9.00	13.06 ± 4.75	12.94 ± 6.16	11.08 ± 4.46
Heart wall	1.71 ± 0.23	1.24 ± 0.06	1.12 ± 0.09	1.03 ± 0.12	0.95 ± 0.11
Kidney	13.57 ± 4.18	6.81 ± 7.57	3.89 ± 1.78	2.73 ± 1.07	1.97 ± 0.61
Liver	16.54 ± 9.53	25.39 ± 4.71	22.54 ± 3.62	18.01 ± 4.68	16.26 ± 4.99
Lung	6.28 ± 0.33	1.97 ± 0.38	1.89 ± 0.33	1.81 ± 0.31	1.78 ± 0.31
Muscle	20.31 ± 3.39	24.84 ± 3.52	28.38 ± 4.23	31.30 ± 4.50	34.01 ± 4.63
Pancreas	1.20 ± 0.16	0.95 ± 0.13	0.78 ± 0.12	0.65 ± 0.17	0.59 ± 0.19
Parotid glands	0.46 ± 0.45	2.25 ± 1.48	2.33 ± 1.50	2.36 ± 1.50	2.47 ± 1.58
Red marrow	8.11 ± 1.23	5.97 ± 1.02	6.06 ± 0.58	6.21 ± 0.49	6.43 ± 0.39
Spleen	1.39 ± 0.35	0.74 ± 0.21	0.71 ± 0.18	0.68 ± 0.20	0.66 ± 0.22
Stomach	0.32 ± 0.15	0.28 ± 0.10	0.23 ± 0.06	0.18 ± 0.03	0.18 ± 0.03
Submandibular glands	0.55 ± 0.48	1.00 ± 0.48	0.99 ± 0.45	0.92 ± 0.39	0.93 ± 0.38
Testes	1.35 ± 0.27	1.02 ± 0.20	0.96 ± 0.16	0.92 ± 0.14	0.91 ± 0.17
Urinary bladder	0.13 ± 0.03	12.47 ± 11.26	21.87 ± 5.55	26.64 ± 5.81	30.87 ± 5.90

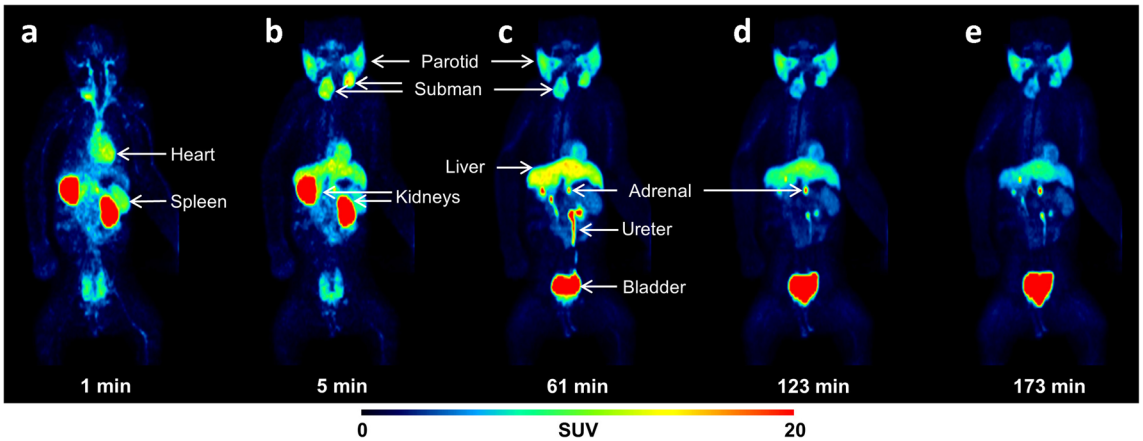

Fig. 2. Representative whole-body PET images of a non-human primate showing the time course of [^{18}F]PFBG after administration of 314 MBq (8.5 mCi) of [^{18}F]PFBG. These maximum intensity projection images in the coronal view show [^{18}F]PFBG uptake at **a** 1 min, **b** 5 min, **c** 61 min, **d** 123 min, and **e** 173 min. The heart, spleen, and the kidneys are clearly delineated within **a** 1-min post injection. Remarkable uptake was noted in the parotids and the submandibular glands (**b**–**e**). The ureter, left adrenal, and bladder are clearly visible on the 61-min image (**c**). With time, the radioactivity levels decreased in the liver and the kidneys whereas the radioactivity levels continued to increase in the bladder (**c**–**e**).

0.13 %ID at 30 min and 0.59 ± 0.19 %ID at 112 min. The uptake in the adrenals was 0.33 ± 0.03 %ID at 30 min and 0.29 ± 0.02 %ID at 112 min. The uptake in the parotid and the submandibular glands was rapid, high, and remained unchanged with time. For example, the average uptake in the parotid gland was 2.25 ± 1.48 %ID and 2.47 ± 1.58 %ID at 30 min and 112 min, respectively ($p > 0.1$). Similarly, accumulation in the submandibular gland at 30 min and 112 min also did not change significantly over time ($p > 0.1$).

Residence times, also referred to as the average number of disintegrations in an organ, were calculated for the source organs that were easily visualized on the PET images and are presented in Table 2. The radiation dose to various organs, EDE, and ED estimates for the 70-kg adult male phantom and other relevant age phantoms were calculated using the 1-h bladder voiding model and selected results are presented in Table 3 along with two other relevant ^{18}F-labeled radiopharmaceuticals. The mean ED for the 70-kg adult and 5-year-old was 0.04 ± 0.00 mSv/MBq, and 0.50 ± 0.08 mSv/MBq, respectively. The organs that received the largest radiation absorbed dose for the 70-kg adult male model were the testes (0.11 ± 0.02 mGy/MBq), adrenals (0.08 ± 0.01 mGy/MBq), and urinary bladder wall (0.08 ± 0.01 mGy/MBq). For the 5-year-old phantom, the organs receiving the largest radiation absorbed dose were the testes (2.26 ± 0.40 mGy/MBq), adrenals (0.30 ± 0.02 mGy/MBq) and urinary bladder wall (0.22 ± 0.03 mGy/MBq). The mean EDE modeled for the 70-kg male and 5-year-old infant was 0.05 ± 0.01 mSv/MBq and 0.64 ± 0.10 mSv/MBq, respectively. Subsequently, we compared ED for [^{18}F]PFBG, 2-deoxy-2-[^{18}F]fluoro-D-glucose, and [*I]MIBG for various age group phantom models (Table 4). As seen from Table 4, the inclusion of testes residence time for OLINDA analysis resulted in 2-fold higher ED for [^{18}F]PFBG than that without the testes residence time.

Discussion

The focus of this work was to assess the whole-body distribution pattern for [^{18}F]PFBG in non-human primates

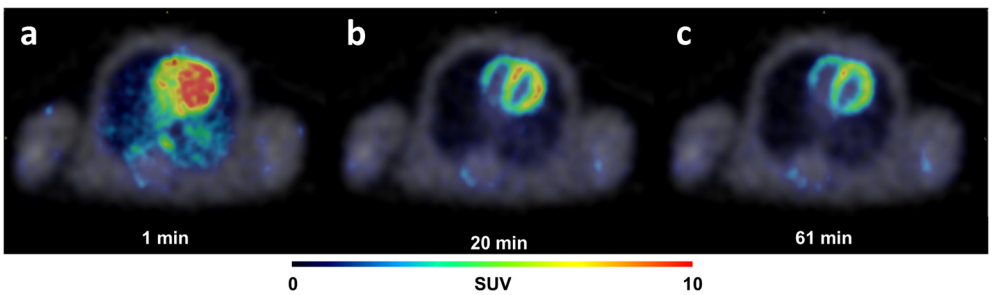

Fig. 3. Axial views of the PET scans fused with the Ge-68 isotope transmission scan show the radioactivity accumulation pattern in the heart over time. The heart is clearly visible soon after the injection and **a** shows a significant blood pool component. By 20 min, **b** the blood pool radioactivity levels have decreased and the septal wall became distinctly visible. The myocardial and septal walls remained distinctly visible thereafter in **c**.

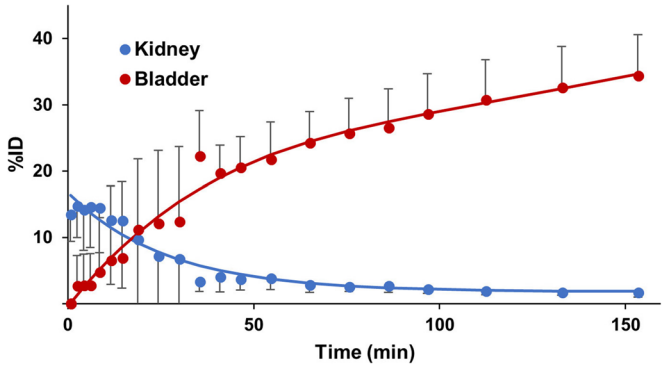

Fig. 4. The time activity curves show the washout of radioactivity from the kidneys and simultaneous accumulation in the bladder. Data points are the mean ± standard deviation determined in three non-human primates and are corrected for radioactive decay. The solid lines represent the best fit curve for each organ. At ~ 5-min post injection, the kidney radioactivity levels fall significantly while the radioactivity levels started to rise in the urinary bladder.

and to estimate human radiation absorbed dose as a prelude to the use of [^{18}F]PFBG in humans. Several PET dosimetry studies have compared the biodistribution and absorbed radiation dose data from humans, non-human primates, or rodents [37–39]. In general, the human dosimetry data calculated from biodistribution results in non-human primates is more accurate and has provided better estimates than those derived from rodents [37]. In this report, we describe whole-body uptake and distribution characteristics of the NET probe [^{18}F]PFBG in primates and provide radiation absorbed dose estimates.

Favorable biodistribution and fast wash-in and wash-out of radioactivity was noted for several key organs which facilitated clear visualization of these organs on the PET images. Intense uptake was noted in the kidneys within 1-min post injection which peaked by 6 min followed by a significant decline in radioactivity levels, thereafter. In contrast, the radioactivity level in the urinary bladder was initially low and increased steadily with time. The rise in radioactivity levels in the bladder coincided with the washout of radioactivity from the kidneys (Fig. 4). This uptake and clearance pattern is consistent with the urinary excretion of hydrophilic ligands and suggests renal clearance as the major route of [^{18}F]PFBG excretion from the body.

In rodent biodistribution studies reported earlier, at 1 h post injection, [^{18}F]PFBG showed 1.2 ± 0.74 %ID/g in the bone [16] which perhaps indicates slight defluorination *in vivo*. The PET images from this study did not show

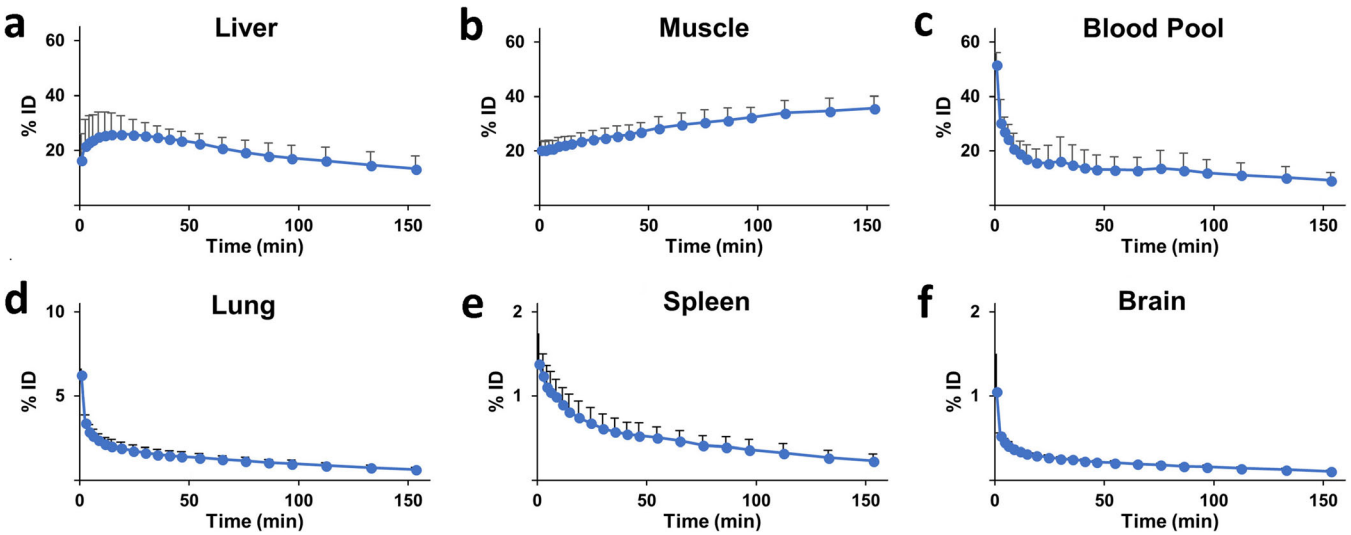

Fig. 5. Time activity curves construed from the whole body PET scans for easily visualized organs: **a** liver, **b** muscle, **c** blood pool, **d** lung, **e** spleen, and **f** brain, after administration of [^{18}F]PFBG. The percent injected dose in organs (%ID) is presented as the mean ± standard deviation from three non-human primate scans and is decay corrected. Initially, liver showed high uptake levels which was followed by a gradual washout of radioactivity. The radioactivity levels in the lungs and brain were low for the duration of the study. While the muscles were not visualized on PET scans, a higher amount of radioactivity (%ID) was noted, primarily due to very large overall muscle mass.

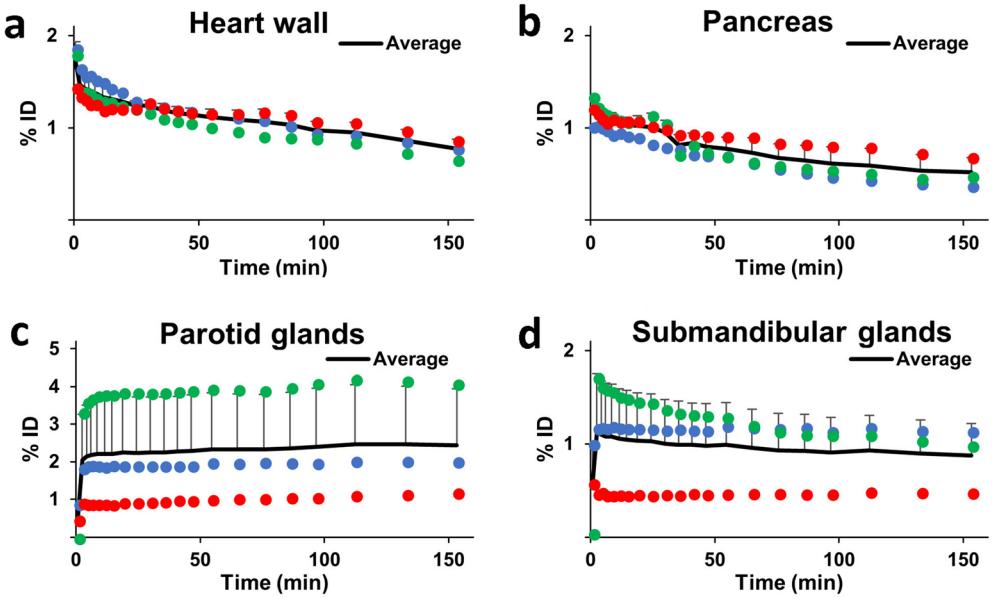

Fig. 6. Time activity curves (TACs) showing the accumulation of [^{18}F]PFBG in **a** the myocardium, **b** pancreas, and **c** parotid, and **d** submandibular glands. Uptake for individual non-human primates is shown by the colored dots while the solid line represents the average value ($n = 3$; mean ± standard deviation). These TACs show rapid accumulation with a sustained retention of radioactivity in these organs.

uptake in the bones which suggests no *in vivo* defluorination in primates within the study time frame. Similarly, other studies conducted previously in canines also did not show bone uptake in the PET images which provides further evidence of the resistance of [^{18}F]PFBG towards *in vivo* defluorination [23]. Although the exact rationale or mechanism for such differences is unknown, many investigators have reported significant differences in distribution and accumulation of radioactivity in rodents and primates, with species difference hypothesized as a plausible cause [20, 23, 40, 41]. Extensive peripheral defluorination of [^{18}F]SP203, a PET probe that targets mGluR5, was observed in rats and not in humans and these differences were assumed to be mediated by the mammalian glutathione transferase activity levels which varies with species and tissues [42–44]. In addition, P450 isoforms and rat serum esterase have also been implicated in divergent metabolic degradation of various compounds between primates and rodents [45]. While the muscles were not discernible on the PET images, the total uptake when calculated as %ID, was very high (32.40 ± 3.60 %ID at 97 min) which could be attributed to relatively high muscle mass (> 2000 g) compared to the mass of other organs that are significantly smaller (liver ~ 200 g, kidneys ~ 40 g).

Table 2.. Residence times for [^{18}F]PFBG in various organs derived from PET images acquired in non-human primates ($n = 3$; mean ± standard deviation)

Organ	Residence time (min)
Adrenals	0.46 ± 0.03
Brain	0.48 ± 0.05
Heart wall	1.54 ± 0.13
Kidney	6.04 ± 3.41
Liver	28.01 ± 7.73
Lung	2.97 ± 0.56
Muscle	49.43 ± 5.75
Pancreas	1.06 ± 0.23
Red marrow	10.01 ± 0.90
Salivary glands	4.94 ± 2.48
Spleen	1.09 ± 0.33
Stomach	0.32 ± 0.07
Testes	1.50 ± 0.26
Urinary bladder	42.28 ± 9.32
Remainder of body	8.33 ± 4.20

At early timepoints, the left adrenal gland was clearly and distinctly visible. Nonetheless, the right adrenal gland remained masked initially, perhaps due to high radioactivity contents in the surrounding tissues such as kidney and liver. As radioactivity levels in liver and kidney dropped, the right adrenal gland became more apparent (Fig. 2). Since the sympathetic nervous system plays a key role in controlling the heart function through modulating the uptake and release of NE in the heart, we evaluated the uptake and washout pattern of [^{18}F]PFBG in the heart. Sustained and persistent uptake with limited washout of [^{18}F]PFBG was noted in the heart among all three primates (Fig. 6). The salivary glands are highly innervated by parasympathetic and sympathetic nerves and has been recognized as an NE uptake site [46]. Intense uptake of [^{131}I]MIBG in the salivary glands has been previously attributed to accumulation in presynaptic adrenergic nerves surrounding the salivary gland cells [47–49]. Therefore, it is reasonable to assume that [^{18}F]PFBG should accumulate in the salivary glands due to dense sympathetic innervation [48, 49]. The results from this study showed

Table 3.. Radiation dose estimates for [^{18}F]FDG, [^{18}F]MFBG, and [^{18}F]PFBG. The radiation dose for [^{18}F]PFBG is derived from PET images of non-human primate using 1 h bladder void model and extrapolated to various age groups (mean ± standard deviation)

Organ	[^{18}F]FDG [35] Adult (mGy/MBq)	[^{18}F]MFBG [22] Adult (mGy/MBq)	[^{18}F]PFBG Adult Male (mGy/MBq)	[^{18}F]PFBG 15 year (mGy/MBq)	[^{18}F]PFBG 5 year (mGy/MBq)
Adrenals	0.01	0.02 ± 0.02	0.08 + 0.01	0.12 ± 0.01	0.25 ± 0.02
Brain	0.04	0.00 ± 0.00	0.00 ± 0.00	0.00 ± 0.00	0.01 ± 0.00
Breasts	0.01	0.01 ± 0.00	0.00 ± 0.00	0.00 ± 0.00	0.01 ± 0.00
Gallbladder wall	0.01	0.01 ± 0.01	0.02 ± 0.00	0.02 ± 0.00	0.04 ± 0.01
Lower large intestine wall	0.01	0.01 ± 0.01	0.01 ± 0.00	0.01 ± 0.00	0.02 ± 0.00
Small intestine	0.01	0.01 ± 0.00	0.01 ± 0.00	0.01 ± 0.00	0.02 ± 0.00
Stomach wall	0.01	0.01 ± 0.00	0.01 ± 0.00	0.01 ± 0.00	0.03 ± 0.00
Upper large intestine wall	0.01	0.01 ± 0.00	0.01 ± 0.00	0.01 ± 0.00	0.02 ± 0.00
Heart wall	0.07	0.03 ± 0.02	0.02 ± 0.00	0.03 ± 0.00	0.06 ± 0.01
Kidneys	0.02	0.03 ± 0.03	0.07 ± 0.03	0.08 ± 0.04	0.17 ± 0.08
Liver	0.02	0.05 ± 0.03	0.06 ± 0.02	0.08 ± 0.02	0.18 ± 0.04
Lungs	0.02	0.01 ± 0.01	0.01 ± 0.00	0.02 ± 0.00	0.04 ± 0.01
Muscle	0.01	0.01 ± 0.00	0.01 ± 0.00	0.01 ± 0.00	0.07 ± 0.01
Ovaries	0.01	0.01 ± 0.01	0.01 ± 0.00	0.01 ± 0.00	0.02 ± 0.00
Pancreas	0.01	0.03 ± 0.02	0.04 ± 0.01	0.06 ± 0.01	0.15 ± 0.03
Red marrow	0.01	0.01 ± 0.00	0.02 ± 0.00	0.02 ± 0.00	0.06 ± 0.00
Osteogenic cells	0.01	0.01 ± 0.00	0.01 ± 0.00	0.02 ± 0.00	0.04 ± 0.00
Skin	0.01	0.00 ± 0.00	0.00 ± 0.00	0.00 ± 0.00	0.01 ± 0.00
Spleen	0.01	0.02 ± 0.01	0.03 ± 0.01	0.04 ± 0.01	0.08 ± 0.02
Testes	0.01	0.01 ± 0.01	0.11 ± 0.02	0.26 ± 0.04	2.26 ± 0.40
Thymus	0.01	0.01 ± 0.00	0.01 ± 0.00	0.01 ± 0.00	0.02 ± 0.00
Thyroid	0.01	0.03 ± 0.03	0.00 ± 0.00	0.01 ± 0.00	0.01 ± 0.00
Urinary bladder wall	0.13	0.19 ± 0.20	0.08 ± 0.01	0.10 ± 0.01	0.22 ± 0.03
Uterus	0.02	NR	0.01 ± 0.00	0.01 ± 0.00	0.03 ± 0.00
Total body	0.01	0.01 ± 0.01	0.01 ± 0.00	0.01 ± 0.00	0.03 ± 0.00
Effective Dose Equivalent (EDE) (mSv/MBq)	NR	NR	0.05 ± 0.01	0.10 ± 0.01	0.64 ± 0.10
Effective dose (ED) (mSv/MBq)	0.02	0.02 ± 0.01	0.04 ± 0.00	0.07 ± 0.01	0.50 ± 0.08

NR not reported

early and sustained levels of [^{18}F]PFBG accumulation in the salivary glands (Fig. 6). While these uptake levels were high and persistent for all three non-human primates in this study, slightly lower uptake was noted in the salivary glands of an older primate ($p < 0.05$) which is likely due to the depleted innervation in the older non-human primate since salivary gland cells degenerate and undergo structural and functional changes with age [50].

We used data from these whole-body PET images to derive EDE and ED estimates for [^{18}F]PFBG for the 70-kg male phantom using the residence times derived from tissue TACs. The fast clearance of [^{18}F]PFBG from most normal organs led to short residence times (Table 2). In addition to the favorable biodistribution pattern, the short half-life of the ^{18}F-radionuclide may have contributed towards these short residence times, which resulted in modest radiation absorbed dose to many organs (Table 3). Recently, the group from Memorial Sloan Kettering published radiation dosimetry estimates for [^{18}F]MFBG [22] through their "first-in-human" study using this radiopharmaceutical. We, therefore, compared the radiation dose estimates for [^{18}F]PFBG with newly reported dose estimates for [^{18}F]MFBG [22] and also with [^{18}F]FDG [35], a widely used PET radiopharmaceutical (Table 3). In most dosimetry calculations, the testes residence time is not included in such analysis, largely due to poor or no visualization of testes on the scans. It is likely that this may have contributed towards a higher ED for [^{18}F]PFBG. Therefore, we further added ED for [^{18}F]PFBG without the testes residence time and presented a head-on comparison of ED for various radiolabeled benzylguanidines

Table 4.. Comparison of Effective Dose for [^{18}F]PFBG (with and without including residence time data for the testes in dosimetry calculations), [^{18}F]FDG, and various [*I]MIBGs

Model	[^{18}F]PFBG (mSv/MBq)	[^{18}F]PFBG w/o testes (mSv/MBq)	[^{18}F]MFBG [22] (mSv/MBq)	[^{18}F]FDG [35] (mSv/MBq)	[^{123}I]MIBG [36] (mSv/MBq)	[^{131}I]MIBG[36] (mSv/MBq)	[^{124}I]MIBG [14] (mSv/MBq)
Adult	0.04	0.02	0.02	0.02	0.02	0.15	0.25
15 year	0.07	0.02	NR	0.02	0.02	0.20	0.39
10 year	0.42	0.03	NR	0.04	0.03	0.25	0.58
5 year	0.50	0.05	NR	0.06	0.04	0.40	1.03
1 year	0.70	0.09	NR	0.10	0.07	0.71	1.92

NR data not reported

in Table 4. We find that the ED for [^{18}F]PFBG (without testes residence times), [^{18}F]MFBG, [^{18}F]FDG, and [^{123}I]MIBG are quite comparable. In contrast, the ED for [^{124}I]MIBG and [^{131}I]MIBG were significantly higher (Table 4). For example, the ED for [^{18}F]PFBG in a 70-kg male (0.02 mSv/MBq) was ~ 12-fold and ~ 7-fold lower than the ED for [^{124}I]MIBG and [^{131}I]MIBG, respectively (Table 4). Since the effective radiation dose is inversely proportional to the body weight/volume, the dose to small children and infants is anticipated to be somewhat higher than that for adults [36, 51, 52]. In this study, the testes was the organ receiving the highest radiation dose. The ED from the CT portion of a PET/CT exam can range from 4 to 75 mSv depending on the imaging protocol and scanner which would be common to most PET radiopharmaceuticals. In summary, the total radiation dose estimated from [^{18}F]PFBG is favorable and comparable to its *meta* analogue [^{18}F]MFBG and to many other radiopharmaceuticals currently used in clinical studies.

Conclusion

Rapid and persistent uptake of [^{18}F]PFBG was noted in NET-rich organs such as the heart and salivary glands. In general, a favorable biodistribution with fast wash-in and wash-out patterns was noted for most normal organs. Renal clearance is the major path for elimination of [^{18}F]PFBG. The radiation dose estimates suggest modest radiation risk in humans, similar to many other radiopharmaceuticals and supports the use of [^{18}F]PFBG for translational and clinical applications. While the uptake and distribution for the two fluorinated benzylguanidines is quite comparable, it is likely that a higher radiochemical yields for [^{18}F]PFBG would influence its preferred use.

Acknowledgments. We would like to thank Kimberly Black, Leah Rutkowski, Andrew Lynch, and Holly Smith for their excellent technical help. Strong support from the Center for Biomolecular Imaging of Wake Forest University Health Sciences is greatly appreciated and acknowledged. All applicable institutional and/or national guidelines for the care and use of animals were followed.

Compliance with Ethical Standards

Conflict of Interest

The authors declare that they have no conflict of interest.

References

1. Altmann A, Kissel M, Zitzmann S, Kübler W, Mahmut M, Peschke P, Haberkorn U (2003) Increased MIBG uptake after transfer of the human norepinephrine transporter gene in rat hepatoma. J Nucl Med 44:973–980
2. Smets LA, Loesberg C, Janssen M, Metwally EA, Huiskamp R (1989) Active uptake and extravesicular storage of m-iodobenzylguanidine in human neuroblastoma SK-N-SH cells. Cancer Res 49:2941–2944
3. Nakajo M, Shapiro B, Copp J, Kalff V, Gross MD, Sisson JC, Beierwaltes WH (1983) The normal and abnormal distribution of the adrenomedullary imaging agent m-[I-131]iodobenzylguanidine (I-131 MIBG) in man: evaluation by scintigraphy. J Nucl Med 24:672–682
4. Wakasugi S, Wada A, Hasegawa Y, Nakano S, Shibata N (1992) Detection of abnormal cardiac adrenergic neuron activity in adriamycin-induced cardiomyopathy with iodine-125-metaiodobenzylguanidine. J Nucl Med 33:208–214
5. Stanton MS, Tuli MM, Radtke NL, Heger JJ, Miles WM, Mock BH, Burt RW, Wellman HN, Zipes DP (1989) Regional sympathetic denervation after myocardial infarction in humans detected noninvasively using I-123-metaiodobenzylguanidine. J Am Coll Cardiol 14:1519–1526
6. Freitas JE (1995) Adrenal cortical and medullary imaging. Semin Nucl Med 25:235–230
7. Shulkin BL, Shapiro B, Francis IR et al (1986) Primary extra-adrenal pheochromocytoma: positive I-123 MIBG imaging with negative I-131 MIBG imaging. Clin Nucl Med 11:851–854
8. Shapiro B, Copp JE, Sisson JC, Eyre PL, Wallis J, Beierwaltes WH (1985) Iodine-131 metaiodobenzylguanidine for the locating of suspected pheochromocytoma: experience in 400 cases. J Nucl Med 26:576–585
9. Sisson JC, Shulkin BL (1999) Nuclear medicine imaging of pheochromocytoma and neuroblastoma. Q J Nucl Med 43:217–223
10. Hanson MW, Feldman JM, Blinder RA, Moore JO, Coleman RE (1989) Carcinoid tumors: iodine-131 MIBG scintigraphy. Radiology 172:699–703
11. Ansari AN, Siegel ME, DeQuattro V, Gazarian LH (1986) Imaging of medullary thyroid carcinoma and hyperfunctioning adrenal medulla using iodine-131 metaiodobenzylguanidine. J Nucl Med 27:1858–1860
12. Feine U, Muller-Schauenburg W, Treuner J, Klingebiel T (1987) Metaiodobenzylguanidine (MIBG) labeled with ^{123}I/^{131}I in neuroblastoma diagnosis and follow-up treatment with a review of the diagnostic results of the International Workshop of Pediatric Oncology held in Rome, September 1986. Med Pediatr Oncol 15:181–187
13. Kuker R, Sztejnberg M, Gulec S (2017) I-124 imaging and dosimetry. Mol Imaging Radionucl Ther 26:66–73
14. Lee CL, Wahnishe H, Sayre GA, Cho HM, Kim HJ, Hernandez-Pampaloni M, Hawkins RA, Dannoon SF, VanBrocklin HF, Itsara M, Weiss WA, Yang X, Haas-Kogan DA, Matthay KK, Seo Y (2010) Radiation dose estimation using preclinical imaging with ^{124}I-metaiodobenzylguanidine (MIBG) PET. Med Phys 37:4861–4867
15. Vaidyanathan G, Affleck DJ, Zalutsky MR (1994) (4-[^{18}F]Fluoro-3-iodobenzyl)guanidine, a potential MIBG analogue for positron emission tomography. J Med Chem 37:3655–3662
16. Garg PK, Garg S, Zalutsky MR (1994) Synthesis and preliminary evaluation of para- and meta-[^{18}F]fluorobenzylguanidine. Nuc Med Biol 21:97–103
17. Zhang H, Huang R, Pillarsetty N, Thorek DLJ, Vaidyanathan G, Serganova I, Blasberg RG, Lewis JS (2014) Synthesis and evaluation of ^{18}F-labeled benzylguanidine analogs for targeting the human norepinephrine transporter. Eur J Nucl Med Mol Imaging 41:322–332
18. Cavallo G, Metrangolo P, Milani R, Pilati T, Priimagi A, Resnati G, Terraneo G (2016) The halogen bond. Chem Rev 116:2478–2601
19. Berry CR, Garg PK, DeGrado TR et al (1994) Para [F-18] fluorobenzylguanidine (PFBG) kinetics in a canine coronary artery occlusion model. J Nucl Med 35:157
20. Berry CR, DeGrado TR, Nutter F et al (2002) Imaging of pheochromocytoma in 2 dogs using p-[^{18}F]fluorobenzylguanidine. Vet Radiol Ultrasound 43:183–186
21. Berry CR, Garg PK, Zalutsky MR, Coleman RE, DeGrado T (1996) Uptake and retention kinetics of para-fluorine-18-fluorobenzylguanidine in isolated rat heart. J Nucl Med 37:2011–2016
22. Pandit-Taskar N, Zanzonico P, Staton KD, Carrasquillo JA, Reidy-Lagunes D, Lyashchenko S, Burnazi E, Zhang H, Lewis JS, Blasberg R, Larson SM, Weber WA, Modak S (2018) Biodistribution and dosimetry of ^{18}F-Meta-Fluorobenzylguanidine: a first-in-human PET/CT imaging study of patients with neuroendocrine malignancies. J Nucl Med 59:147–153
23. Berry CR, Garg PK, DeGrado TR et al (1996) Para-[^{18}F]fluorobenzylguanidine kinetics in a canine coronary artery occlusion model. J Nucl Cardiol 3:119–129
24. Moroz MA, Serganova I, Zanzonico P, Ageyeva L, Beresten T, Dyomina E, Burnazi E, Finn RD, Doubrovin M, Blasberg RG (2007) Imaging hNET reporter gene expression with ^{124}I-MIBG. J Nucl Med 48:827–836
25. DeGrado TR, Turkington TG, Williams JJ, Stearns CW, Hoffman JM, Coleman RE (1994) Performance characteristics of a whole-body PET scanner. J Nucl Med 35:1398–1406

26. Lewellenm TK, Kohlmyer SG, Miyaoka RS et al (1996) Investigation of the performance of the General Electric ADVANCE positron emission tomograph in 3D mode. IEEE Trans Nucl Sc 43:2199–2206
27. Lewellen TK, Kohlmyer SG, Miyaoka RS, Schubert S, Stearns CW (1995) Investigation of the count rate performance of general electric advance positron emission tomograph. IEEE Trans Nucl Sc 42:1051–1057
28. Kinahan PE, Townsend DW, Beyer T, Sashin D (1998) Attenuation correction for a combined 3D PET/CT scanner. Med Phys 25:2046–2053
29. Kinahan PE, Rogers JG (1989) Analytical 3D image reconstruction using all detected events. IEEE Trans Nucl Sci 36:964–968
30. Valentin J (2002) ICRP-89: basic anatomical and physiological data for use in radiological protection reference values. Ann ICRP 32
31. Garg PK, Lokitz SJ, Nazih R, Garg S (2017) Biodistribution and radiation dosimetry of 11C-nicotine from whole-body PET imaging in humans. J Nucl Med 58:473–478
32. Makita T, Yamoto T, Ogawa K et al (1984) Body and organ weights of *Macaca fuscata* and *Macaca cyclopis*. Nihon Juigaku Zasshi 46:385–390
33. Mejia AA, Nakamura T, Masatoshi I, Hatazawa J, Masaki M, Watanuki S (1991) Estimation of absorbed doses in humans due to intravenous administration of fluorine-18-fluorodeoxyglucose in PET studies. J Nucl Med 32:699–706
34. Stabin MG, Sparks RB, Crowe E (2005) OLINDA/EXM: the second-generation personal computer software for internal dose assessment in nuclear medicine. J Nucl Med 46:1023–1027
35. ICRP-106 (2008) Radiation dose to patients from radiopharmaceuticals. Addendum 3 to ICRP publication 53. Ann ICRP 106(38):1–197
36. Stabin MG, Gelfand MJ (1998) Dosimetry of pediatric nuclear medicine procedures. Q J Nucl Med 42:93–112
37. Brown AK, Fujita M, Fujimura Y, Liow JS, Stabin M, Ryu YH, Imaizumi M, Hong J, Pike VW, Innis RB (2007) Radiation dosimetry and biodistribution in monkey and man of ^{11}C-PBR28: a PET radioligand to image inflammation. J Nucl Med 48:2072–2079
38. Doss M, Kolb HC, Zhang JJ, Belanger MJ, Stubbs JB, Stabin MG, Hostetler ED, Alpaugh RK, von Mehren M, Walsh JC, Haka M, Mocharla VP, Yu JQ (2012) Biodistribution and radiation dosimetry of the integrin marker ^{18}F-RGD-K5 determined from whole-body PET/CT in monkeys and humans. J Nucl Med 53:787–795
39. Dence CS, Laforest R, Sun X, Sharp TL, Welch MJ, Mach RH (2010) Radiochemical synthesis, rodent biodistribution and tumor uptake, and dosimetry calculations of [^{11}C] methylated LY2181308. Mol Imaging Biol 12:608–615
40. Bonasera TA, O'Neil JP, Xu M, Dobkin JA, Cutler PD, Lich LL, Choe YS, Katzenellenbogen JA, Welch MJ (1996) Preclinical evaluation of fluorine-18-labeled androgen receptor ligands in baboons. J Nucl Med 37:1009–1015
41. Jahan M, Eriksson O, Johnstrom P et al (2011) Decreased defluorination using the novel beta-cell imaging agent [^{18}F]FE-DTBZ-d4 in pigs examined by PET. EJNMMI Res 1:33
42. Lash LH, Qian W, Putt DA, Jacobs K, Elfarra AA, Krause RJ, Parker JC (1998) Glutathione conjugation of trichloroethylene in rats and mice: sex-, species-, and tissue-dependent differences. Drug Metab Dispos 26:12–19
43. Cannady EA, Chien C, Jones TM, Borel AG (2006) In vitro metabolism of the epoxide substructure of cryptophycins by cytosolic glutathione S-transferase: species differences and stereoselectivity. Xenobiotica 36:659–670
44. Shetty HU, Zoghbi SS, Simeon FG et al (2008) Radiodefluorination of 3-fluoro-5-(2-(2-[^{18}F](fluoromethyl)-thiazol-4-yl)ethynyl)benzonitrile ([^{18}F]SP203), a radioligand for imaging brain metabotropic glutamate subtype-5 receptors with positron emission tomography, occurs by glutathionylation in rat brain. J Pharmacol Exp Ther 327:727–735
45. Godin SJ, Crow JA, Scollon EJ, Hughes MF, DeVito MJ, Ross MK (2007) Identification of rat and human cytochrome p450 isoforms and a rat serum esterase that metabolize the pyrethroid insecticides deltamethrin and esfenvalerate. Drug Metab Dispos 35:1664–1671
46. Lee CM, Javitch JA, Snyder SH (1983) Recognition sites for norepinephrine uptake: regulation by neurotransmitter. Science 220:626–629
47. Jentzen W, Richter M, Poeppel TD, Schmitz J, Brandau W, Bockisch A, Binse I (2017) Discrepant salivary gland response after radioiodine and MIBG therapies. Q J Nucl Med Mol Imaging 61:331–339
48. Nakajo M, Shapiro B, Sisson JC, Swanson DP, Beierwaltes WH (1984) Salivary gland accumulation of meta-[^{131}I]iodobenzylguanidine. J Nucl Med 25:2–6
49. Sisson JC, Wieland DM, Jaques S Jr et al (1987) Radiolabeled meta-iodobenzylguanidine and the adrenergic neurons of salivary glands. Am J Physiol Imaging 2:1–9
50. Kim SK, Allen ED (1994) Structural and functional changes in salivary glands during aging. Microsc Res Tech 28:243–253
51. Huda W, Vance A (2007) Patient radiation doses from adult and pediatric CT. AJR Am J Roentgenol 188:540–546
52. Huda W, Scalzetti EM, Roskopf M (2000) Effective doses to patients undergoing thoracic computed tomography examinations. Med Phys 27:838–844